

Saliency Transformation Network: Incorporating Multi-stage Visual Cues for Pancreas Segmentation

Qihang Yu¹, Lingxi Xie², Yan Wang², Yuyin Zhou², Elliot K. Fishman³, Alan L. Yuille²

¹Department of Computer Science, Peking University, Beijing 100084, China

²Department of Computer Science, The Johns Hopkins University, Baltimore, MD 21218, USA

³Department of Radiology, The Johns Hopkins School of Medicine, Baltimore, MD 21287, USA

Abstract

We aim at segmenting small organs (*e.g.*, the pancreas) from abdominal CT scans. As the target often occupies a relatively small region in the input image, deep neural networks can be easily confused by the complex and variable background. To alleviate this, researchers proposed a coarse-to-fine approach (Zhou et al. 2016), which used prediction from the coarse stage to shrink the input region provided to the fine stage. Although this strategy achieves high accuracy, we note that the coarse-scaled and fine-scaled networks were trained and tested individually, which limited the use of multi-stage visual cues for segmentation.

This paper presents a **Saliency Transformation Network**, which contains a trainable *saliency transformation module*. This module computes spatial weights from the coarse-scaled segmentation score map, and applies them to the fine-scaled input image. In training, the coarse-scaled and fine-scaled segmentation networks are optimized in a joint manner, so that both networks become more powerful when they are evaluated individually. In testing, this strategy makes full use of the segmentation results at the coarse stage, so that we can deliver complementary information to the fine stage rather than merely providing a bounding box. We perform experiments on the NIH pancreas segmentation dataset with 82 CT volumes. Following the same testing process which involves a coarse-to-fine iteration, our approach outperforms the state-of-the-art approach (trained in a stage-wise manner) by an average of over 2%. In addition, our approach enjoys better convergence properties, making it more reliable in practice.

Introduction

This paper focuses on small organ (*e.g.*, the pancreas) segmentation from abdominal CT scans, which is an important prerequisite for enabling computers to assist human doctors for clinical purposes. This falls into a research area named *medical imaging analysis*. Recently, great progress has been brought to this field by the fast development of deep learning, especially the convolutional neural networks (Krizhevsky, Sutskever, and Hinton 2012)(Long, Shelhamer, and Darrell 2015). Many conventional methods, such as the graph-based segmentation approaches (Ali, Farag, and El-Baz 2007) or those frameworks based on handcrafted local features (Wang et al. 2014), have been

Copyright © 2018, Association for the Advancement of Artificial Intelligence (www.aaai.org). All rights reserved.

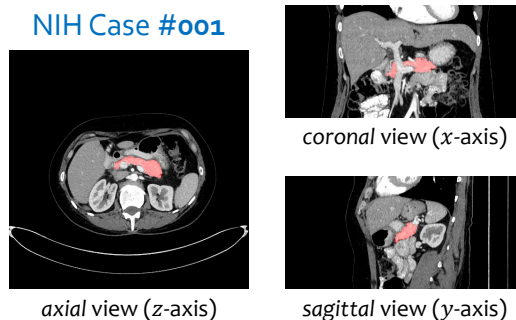


Figure 1: An typical example from the NIH pancreas segmentation dataset (Roth et al. 2015). We visualize the pancreas in red along three different viewpoints (best viewed in color). It is a relatively small organ with an irregular shape.

replaced by the deep neural networks, which typically produce higher segmentation accuracy (Ronneberger, Fischer, and Brox 2015)(Roth et al. 2015).

The pancreas is a small organ which suffers from substantial variance in its shape, size and location. As it often occupies a small fraction of input data (*e.g.*, less than 0.5% in a 2D image), deep segmentation networks such as FCN (Long, Shelhamer, and Darrell 2015) can be easily confused by the background region which may contain complicated and variable contents. Motivated by the idea that using rough localization to shrink the input region, researchers proposed a coarse-to-fine approach (Zhou et al. 2016) with two (coarse and fine) stages. Despite the state-of-the-art performance achieved in pancreas segmentation, we note that this approach trained and tested these two stages in an individual manner, making it very difficult for them to communicate with each other. As an example, in the testing process, the fine stage only receives a bounding box from the coarse-scaled segmentation, while the pixel-wise score map which contains rich information, especially around the boundary, is mostly discarded.

In this paper, we present an effective framework named the **Saliency Transformation Network**. The chief novelty is to insert a learnable transformation module between two stages. This module summarizes the coarse-scaled segmen-

tation scores into a spatial weighting map and applies it to the fine stage. Despite its simplicity, adding this module brings us two advantages. First, the coarse-scaled and fine-scaled networks can be trained in a joint manner, which is verified to improve the segmentation ability of each of them. Second, the coarse-scaled segmentation scores can be delivered to the fine stage, so that multi-stage visual cues are incorporated through the entire coarse-to-fine iteration. Experiments are performed on the NIH pancreas segmentation dataset (Roth et al. 2015). Following the same testing flowchart of (Zhou et al. 2016), *i.e.*, one coarse-scaled segmentation followed by an iterative process of fine-scaled segmentations, we outperform the stage-wise approach (the state-of-the-art) by more than 2%, measured by the average Dice-Sørensen coefficient (DSC). We also verify better convergence which guarantees the reliability of our approach.

The remainder of this paper is organized as follows. The following sections briefly review related work to this paper, and illustrate the proposed framework. After experiments are displayed, we draw our conclusions in the final part.

Related Work

Computer-aided diagnosis (CAD) is an important technique which can assist human doctors in many clinical scenarios. An important prerequisite of CAD is medical imaging analysis. As a popular and cheap way of medical imaging, contrast-enhanced computed tomography (CECT) produces detailed images of internal organs, bones, soft tissues and blood vessels. It is of great value to automatically segment organs and/or soft tissues from these CT volumes for further diagnosis (Wang et al. 2016)(Havaei et al. 2017)(Zhou et al. 2017). As different target organs have specific properties such as appearance, shape and anatomical variability, researchers often design an individualized technique for each of them. Typical examples include the liver (Ling et al. 2008)(Heimann et al. 2009), the spleen (Linguraru et al. 2010), the kidneys (Lin, Lei, and Hung 2006)(Ali, Farag, and El-Baz 2007), the lungs (Hu, Hoffman, and Reinhardt 2001), the pancreas (Wang et al. 2014), *etc.* Among these organs, the pancreas is one of the most challenging cases (Roth et al. 2015), arguably because its large anatomical variability, such as low contrast, variable size and irregular shape.

Compared to the above literatures which used conventional approaches for segmentation, the development of deep learning brings much more powerful yet efficient solutions. In particular, the convolutional neural networks have been widely applied to a wide range of vision tasks, such as image classification (Krizhevsky, Sutskever, and Hinton 2012)(Simonyan and Zisserman 2015)(He et al. 2016), object detection (Girshick et al. 2014)(Ren et al. 2015), and semantic segmentation (Long, Shelhamer, and Darrell 2015)(Chen et al. 2015). In the area of medical imaging analysis, in particular organ segmentation, these techniques have been verified to significantly outperform conventional approaches, *e.g.*, segmenting the liver (Dou et al. 2016), the lung (Harrison et al. 2017), or the pancreas (Roth et al. 2016)(Cai et al. 2017)(Roth et al. 2017). Note that medical images differ from natural images in that data appear in a volumetric (3D) form. To deal with this challenge, researchers either slice the

3D volume into 2D slices (as in this work), or train a 3D-based network directly (Kamnitsas et al. 2016)(Merkow et al. 2016)(Milletari, Navab, and Ahmadi 2016). In the latter case, due to the limit in GPU memory, the networks often take local patches as input data. The tradeoff between 2D and 3D approaches were discussed in (Lai 2015).

In comparison to the entire CT volume, the target organ often occupies a relatively small area. As the deep segmentation networks such as FCN (Long, Shelhamer, and Darrell 2015) are less accurate in depicting small targets, researchers proposed two types of ideas to improve detection and/or segmentation performance. The first one involved rescaling the image so that the target becomes comparable to the training samples (Xia et al. 2016), and the second one considered shrinking the input region with respect to each target to obtain higher detection (Chen et al. 2016a) or better segmentation (Zhang et al. 2016) accuracy. This work is based on recent work (Zhou et al. 2016) which designed a coarse-to-fine segmentation framework. We connect the coarse and fine stages via a saliency transformation module, which allows joint optimization and enables useful information to be propagated between these two stages.

Our Approach

Problem and Baseline

Let a CT-scanned image be a 3D volume \mathbf{X} of size $W \times H \times L$ which is annotated with a binary ground-truth segmentation \mathbf{Y} where $y_i = 1$ indicates a foreground voxel. The goal of our work is to produce a binary output volume \mathbf{Z} of the same dimension. Denote \mathcal{Y} and \mathcal{Z} as the set of foreground voxels in the ground-truth and prediction, *i.e.*, $\mathcal{Y} = \{i \mid y_i = 1\}$ and $\mathcal{Z} = \{i \mid z_i = 1\}$. The accuracy of segmentation is evaluated by the Dice-Sørensen coefficient (DSC): $\text{DSC}(\mathcal{Y}, \mathcal{Z}) = \frac{2 \times |\mathcal{Y} \cap \mathcal{Z}|}{|\mathcal{Y}| + |\mathcal{Z}|}$. This metric falls in the range of $[0, 1]$ with 1 implying perfect prediction.

Our baseline approach was presented in (Zhou et al. 2016). It applied 2D-based deep networks for 3D segmentation, which was verified both effective and efficient. Each 3D volume \mathbf{X} was sliced along three axes, *i.e.*, the *coronal*, *sagittal* and *axial* views, and these 2D slices were denoted as $\mathbf{X}_{C,w}$ ($w = 1, 2, \dots, W$), $\mathbf{X}_{S,h}$ ($h = 1, 2, \dots, H$) and $\mathbf{X}_{A,l}$ ($l = 1, 2, \dots, L$), where the subscripts C, S and A stood for *coronal*, *sagittal* and *axial*, respectively. On each axis, an individual 2D-FCN (Long, Shelhamer, and Darrell 2015) was trained for segmentation. These models were denoted as \mathbb{M}_C , \mathbb{M}_S and \mathbb{M}_A , respectively. We also follow (Zhou et al. 2016) in other technical details, *e.g.*, the DSC loss function was used in the training stage to prevent the models from being biased towards the background class, and both multi-slice segmentation and multi-axis fusion were performed to make use of 3D information in 2D-based networks.

Motivation

The pancreas is a relatively small organ. In each 2D slice, the fraction of the pancreas pixels is often smaller than 1.5%. To prevent deep networks such as FCN (Long, Shelhamer, and Darrell 2015) from being confused by the complicated and variable background contents, (Zhou et al. 2016) proposed to

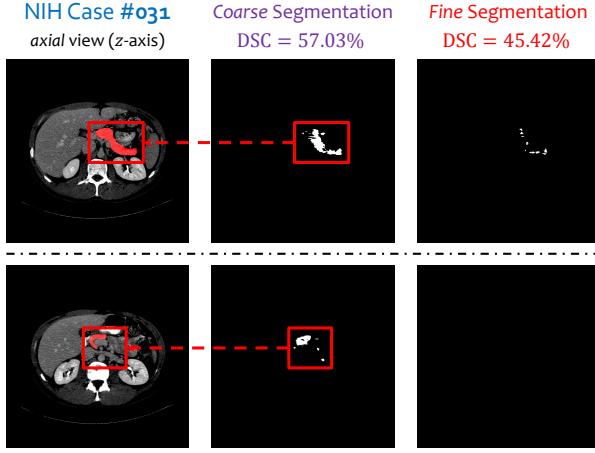


Figure 2: Typical segmentation results (best viewed in color) from the stage-wise approach (Zhou et al. 2016). The red mask on each image slice indicates the ground-truth segmentation, and the red frames represent the shrunk input region. In both slices, poor segmentation is produced at the fine stage, since a small input region loses much information. This can be improved via incorporating coarse-scaled information, as we show in Figure 4.

shrink the input region according to the estimated region of the pancreas. On each viewpoint, two networks were trained, one for the coarse-scaled segmentation and the other for the fine-scaled segmentation. In the testing process, the coarse-scaled network was first used to obtain rough segmentation from the entire 2D image, and the fine-scaled network was executed several times, so that the segmentation mask was improved iteratively until convergence.

This coarse-to-fine approach was verified to improve segmentation accuracy significantly, especially in the scenario of unsatisfying coarse-scaled segmentation. But we notice a drawback. The coarse-scaled and fine-scaled networks were trained and tested individually, which makes it impossible to propagate useful information across different stages. From another perspective, as pixel-wise prediction was made at the coarse stage, it is a major information loss that only a bounding box is computed and used at the fine stage. In some cases, the fine-scaled segmentation is unsatisfying because the shrunk input region is too small, and a possible solution is to incorporate the coarse-scaled segmentation results derived from the entire image. A typical example is shown in Figure 2. This motivates us to connect the coarse and fine stages via a saliency transformation module, which preserves saliency obtained from the coarse stage to obtain more accurate segmentation results at the fine stage.

Formulation

Our approach works on 2D image slices, and we train individual models on three different viewpoints. Without loss of generality, we consider a 2D slice along the *axial* view, denoted as $\mathbf{X}_{A,l}^C$, where the subscript A indicates the *axial* view, l is the index, and the superscript C stands for

the coarse stage (F for the fine stage). $\mathbf{X}_{A,l}^C$ is the coarse-scaled input image. Similarly, the coarse-scaled segmentation result (score map), the fine-scaled input and the fine-scaled segmentation result are denoted as $\mathbf{Z}_{A,l}^C$, $\mathbf{X}_{A,l}^F$ and $\mathbf{Z}_{A,l}^F$, respectively. The coarse-scaled and fine-scaled networks are denoted as $\mathbf{Z}_{A,l}^C = \mathbf{f}^C[\mathbf{X}_{A,l}^C; \theta^C]$ and $\mathbf{Z}_{A,l}^F = \mathbf{f}^F[\mathbf{X}_{A,l}^F; \theta^F]$, respectively, where $\mathbf{f}^C[\cdot; \theta^C]$ and $\mathbf{f}^F[\cdot; \theta^F]$ are deep convolutional neural networks, with θ^C and θ^F being network parameters.

Our goal is to propagate the segmentation results obtained from the coarse stage to the fine stage. This is implemented via relating $\mathbf{X}_{A,l}^F$ to $\mathbf{Z}_{A,l}^C$. We follow (Zhou et al. 2016) to crop $\mathbf{X}_{A,l}^F$ from $\mathbf{X}_{A,l}^C$, but, before cropping, we multiply each pixel of $\mathbf{X}_{A,l}^C$ by a spatial weight related to the coarse-scaled segmentation score map $\mathbf{Z}_{A,l}^C$. This relationship is formulated by a *saliency transformation function*, which will be detailed below. In summary, $\mathbf{X}_{A,l}^F$ can be written as

$$\mathbf{X}_{A,l}^F = \text{Crop}[\mathbf{X}_{A,l}^C \otimes \mathbf{g}(\mathbf{Z}_{A,l}^C; \theta^T); \mathbf{Z}_{A,l}^C]. \quad (1)$$

Here, $\mathbf{g}(\cdot; \theta^T)$ is the saliency transformation function, θ^T are the parameters, and \otimes denotes element-wise product. The cropping operation $\text{Crop}[\cdot; \mathbf{Z}_{A,l}^C]$ shrinks the weighted input image with respect to the *reference score map* $\mathbf{Z}_{A,l}^C$. Following (Zhou et al. 2016), cropping is performed by binarizing $\mathbf{Z}_{A,l}^C$ with a threshold of 0.5, finding the minimal rectangle covering all the activated pixels, and adding a K -pixel-wide margin (padding) around it.

The saliency transformation function $\mathbf{g}[\cdot, \theta^T]$ needs to satisfy two conditions, namely, it has the same dimensionality as $\mathbf{X}_{A,l}^C$, and is differentiable, so that the coarse-scaled and fine-scaled networks can be optimized in a joint manner. As $\mathbf{X}_{A,l}^C$ and $\mathbf{Z}_{A,l}^C$ share the same dimension, we set $\mathbf{g}[\cdot, \theta^T]$ to be a *size-preserved* convolution operation, which allows the weight added to each pixel to be determined by the segmentation scores in a small neighborhood around it. As we will visualize in the experimental section (see Figure 4), the convolutional kernels deliver complementary information from the coarse stage to the fine stage.

We compute the DSC loss terms for both the coarse-scaled and fine-scaled segmentation, and denote them as $\mathcal{L}\{\mathbf{Y}_{A,l}, \mathbf{Z}_{A,l}^C\}$ and $\mathcal{L}\{\mathbf{Y}_{A,l}, \mathbf{Z}_{A,l}^F\}$, respectively. Here, $\mathbf{Y}_{A,l}$ is the ground-truth segmentation mask, and $\mathcal{L}\{\mathbf{Y}, \mathbf{Z}\} = 1 - \frac{2 \times \sum_i Y_i Z_i}{\sum_i Y_i + \sum_i Z_i}$ is based on a *soft* version of DSC. The goal is to minimize the overall loss:

$$\mathcal{L} = \lambda \cdot \mathcal{L}\{\mathbf{Y}_{A,l}, \mathbf{Z}_{A,l}^C\} + (1 - \lambda) \cdot \mathcal{L}\{\mathbf{Y}_{A,l}, \mathbf{Z}_{A,l}^F\}. \quad (2)$$

This is a joint optimization over both stages, *i.e.*, networks. λ is the parameter to balance between coarse-scaled and fine-scaled segmentation. We set λ to be 1/3 so as to encourage accurate fine-scaled segmentation.

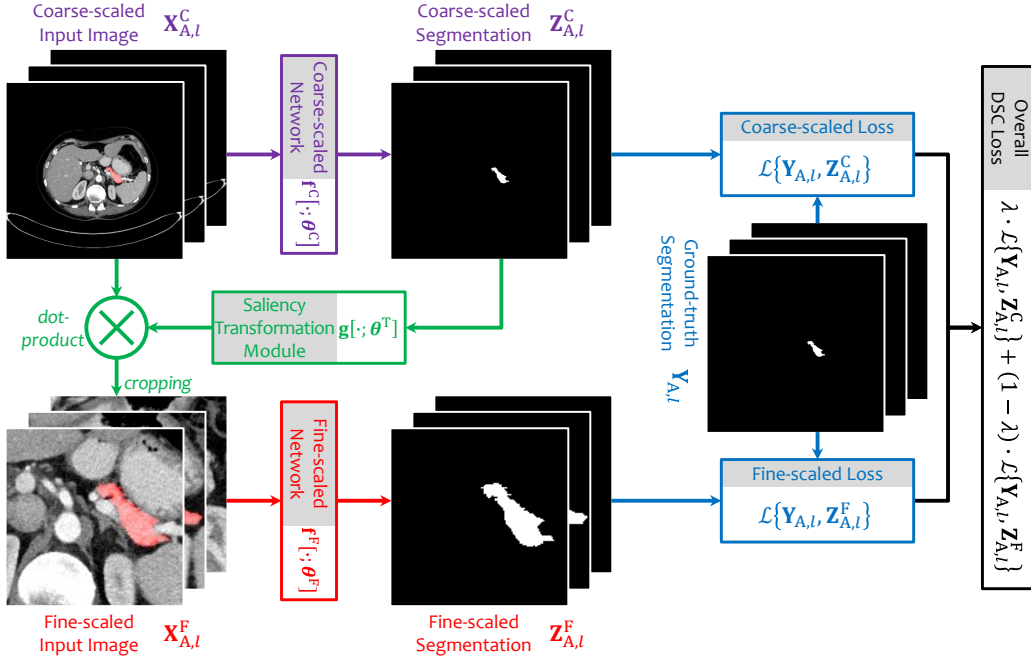


Figure 3: Illustration of the saliency transformation network (best viewed in color). Following (Zhou et al. 2016), we display an example in the *axial* view, which contains 3 neighboring slices. During testing, this model is decomposed into three parts, *i.e.*, the coarse-scaled network, the saliency transformation module, and the fine-scaled network.

Training and Testing

The overall framework of our approach is illustrated in Figure 3. A major difference between these two processes is the source of the reference score map. In the training process, in order to provide high-quality data to the fine-scaled segmentation network, we use the ground-truth segmentation mask $Y_{A,l}$ during image cropping. This weakens the necessity of performing iteration, which mainly changes the cropped region, so we perform the fine-scaled segmentation only once in the training process.

- **In the training phase**, we aim at minimizing the loss function (2). This is straightforward, as the loss function \mathcal{L} is differentiable over all parameters. Such joint optimization is individually performed on three viewpoints, *i.e.*, the *coronal*, *sagittal* and *axial* views.
- **In the testing phase**, we follow (Zhou et al. 2016) to launch an iterative process for coarse-to-fine segmentation. As the ground-truth segmentation mask $Y_{A,l}$ is not available, the coarse-scaled segmentation $Z_{A,l}$ is used for image cropping. If the coarse stage predicts an empty mask on an image slice, the fine stage will not be executed at all, although this slice may actually contain a part of the target organ. To deal with, we fuse segmentation results from three viewpoints after *each* iteration, so that the missing pixels from one network can be recovered via the help of the other two networks.

Technically, each trained model is decomposed into three parts, namely, the coarse-scaled segmentation network, the

saliency transformation module and the fine-scaled segmentation network. When an testing image comes, it is first fed into the coarse-scaled segmentation networks, and the segmentation score maps of three viewpoints are averaged as coarse-scaled segmentation. We perform at most $T = 10$ rounds to refine the initial segmentation mask. In each round, the saliency transformation function is computed via the mask from the previous round, and the fine-scaled segmentation is performed over three viewpoints and then averaged. We follow previous work (Zhou et al. 2016) to terminate the iteration when the inter-iteration DSC, *i.e.*, the DSC between volumes from neighboring iterations, is higher than a given threshold t , *e.g.*, $t = 0.95$. The value of t depends on convergence properties during iteration, and we will investigate this issue in the experimental section.

Comparison to Previous Work

Our method is directly motivated by (Zhou et al. 2016), in which the coarse-scaled and fine-scaled segmentation models were trained individually. By designing a new framework, we enable joint training and thus facilitate these two stages to communicate, leading to improved segmentation accuracy (see the experimental section). Similarly, a stage-wise detection method is proposed in (Chen et al. 2016a) for metosis detection, and we believe that our framework can be generalized to this problem and achieve better detection accuracy.

Another related work is (Zhang et al. 2016). It stacks two FCN’s for segmentation, where the second FCN takes the output score map of the first FCN as a part of its input.

Model	Accuracy (%)	Max DSC (%)	Min DSC (%)
Stage-wise segmentation (Zhou et al. 2016)	82.37 ± 5.68	90.85	62.43
Using 1×1 kernels in saliency transformation	82.85 ± 6.68	90.40	53.44
Using 3×3 kernels in saliency transformation	83.47 ± 5.78	90.63	57.85
Using 5×5 kernels in saliency transformation	83.64 ± 5.29	90.35	66.35
Two-layer saliency transformation (3×3 kernels)	83.93 ± 5.43	90.52	64.78
Fine-tuning with noisy data (3×3 kernels)	83.99 ± 5.09	90.57	65.05

Table 1: Evaluation of different settings of the saliency transformation network. Please see the texts in the experimental section for the detailed descriptions of these variants.

Our work differs from it by (i) we decompose each trained model into two networks and allow iteration in the testing process, and (ii) we shrink the input region with a cropping operation, which is a major contribution to segmentation accuracy. As a result, (Zhang et al. 2016) reported merely an average accuracy of 77.89%. Even with *only one iteration*, we achieve 82.73% and (Zhou et al. 2016) reported 82.16%.

Our approach is also related to a family of attention-based models in computer vision. However, by making use of the properties that (i) an organ often occupies one continuous region in an image slice and (ii) the size of an organ is relatively consistent, it is possible not to introduce complicated modules, such as those in (Chen et al. 2016b)(Xia et al. 2016), for scale invariance in generic object segmentation.

Experiments

Dataset and Evaluation

We evaluate our approach on the NIH pancreas segmentation dataset (Roth et al. 2015), which contains 82 contrast-enhanced abdominal CT volumes. The resolution of each CT scan is $512 \times 512 \times L$, where $L \in [181, 466]$ is the number of sampling slices along the long axis of the body. The distance between neighboring voxels ranges from 0.5mm to 1.0mm.

Following the standard cross-validation strategy, we split the dataset into 4 fixed folds, each of which contains approximately the same number of samples. We apply cross validation, *i.e.*, training the models on 3 out of 4 subsets and testing them on the remaining one. We measure the segmentation accuracy by computing the Dice-Sørensen coefficient (DSC) for each sample, and report the average and standard deviation over all 82 cases.

Different Settings

We use the FCN-8s model (Long, Shelhamer, and Darrell 2015) which was verified successful on natural image segmentation. To fit our task, we reset the up-sampling parts, set the learning rate to be 10^{-4} and perform 80,000 iterations. We also set different options, which differ from each other in the size of convolutional kernels, whether to smooth the segmentation score map, and whether to fine-tune the basic models with images cropped from the coarse-scaled segmentation mask. The quantitative segmentation results of these models are summarized in Table 1.

- **Different receptive field sizes in saliency transformation.** We evaluate 1×1 , 3×3 and 5×5 convolutional

kernels. In general, a moderate kernel size leads to higher segmentation accuracy, as the spatial weights are computed via referring to more information. However, as we turn to 7×7 kernels, the segmentation accuracy is slightly lower than that using 5×5 . In addition, larger kernels require an increasing number of parameters and heavier computational overheads.

- **Using a two-layer saliency transformation function.** An alternative way of increasing the receptive field of the saliency transformation is to use two stacked convolutional layers. In practice, inserting another 3×3 convolutional layer right after the segmentation score map improves accuracy, but we do not continue adding more layers, as the performance seems to saturate, and increasing complexity is risky.
- **Fine-tuning the models with images cropped from the coarse-scaled segmentation mask.** As we use the ground-truth mask in the training process, but use the coarse-scaled segmentation mask in the testing process, this may result in over-fitting as the training and testing data come from different *domains*. To deal with, we fine-tune these models with a smaller learning rate of 10^{-6} and 40,000 more iterations, and use the coarse-scaled segmentation mask to crop the fine-scaled training image during this process. This strategy produces higher segmentation accuracy and, as shown later, alleviates the issue of over-fitting.

In the later experiments, we will use the best parameters learned from the above variants, *i.e.*, using 5×5 convolutional kernels, two stacked convolutional layers for saliency transformation, and fine-tuning the entire framework with images cropped from the coarse-scaled segmentation mask. Note that all these modifications do not bring significant computational overheads in the testing process.

Comparison to the State-of-the-Art

Next, we show that our approach works better than the baseline, *i.e.*, the coarse-to-fine approach with two stages trained individually (Zhou et al. 2016). As shown in Table 2, the average improvement over 82 cases is 2.13%, which is impressive given such a high baseline accuracy (82.37% is already the state-of-the-art). A case-by-case study reveals that our approach reports a higher accuracy on 67 out of 82 cases, and the largest advantage is +17.60% (in comparison, the largest disadvantage is merely -3.85%). In particular,

Approach	Accuracy (%)	Max DSC (%)	Min DSC (%)
(Roth et al. 2015)	71.42 \pm 10.11	86.29	23.99
(Roth et al. 2016)	78.01 \pm 8.20	88.65	34.11
(Zhang et al. 2016)	77.89 \pm 8.52	89.17	43.67
(Roth et al. 2017)	81.27 \pm 6.27	88.96	50.69
(Zhou et al. 2016)	82.37 \pm 5.68	90.85	62.43
(Cai et al. 2017)	82.4 \pm 6.7	90.1	60.0
Ours, one single model	84.50 \pm 4.97	91.02	62.81

Table 2: Comparison to the state-of-the-art approaches on the NIH pancreas segmentation dataset (Roth et al. 2015). The numbers of (Zhang et al. 2016) are based on the re-implementation in (Zhou et al. 2016).



Figure 4: Visualization of how the saliency transformation module works in coarse-to-fine segmentation (best viewed in color). Poor segmentation results are produced by the stage-wise approach, but this can be prevented via using the segmentation score map from the previous round to guide the next round during iteration. In each round, the three weight maps capture different visual cues, with two of them focused on the foreground region, and the remaining one focused on the background region.

our approach also reports a reasonable accuracy on the worst testing case, suggesting stronger reliability.

Finally, we compare our results with several recent publications. Table 2 shows that our approach outperforms all literatures including those published recently. Note that our approach enjoys high efficiency. On a Titan-X Pascal GPU, our approach requires around 1.3 minute on each testing case, which is comparable to the baseline (Zhou et al. 2016) (0.9 minutes), and much faster than several other competitors (Roth et al. 2015)(Roth et al. 2016).

Incorporating Multi-stage Visual Cues

We first visualize the spatial weights added by the saliency transformation module. A typical example is displayed in Figure 4. We can see that three different channels deliver complementary information, *i.e.*, two of them focus on the foreground of the target organ, and the remaining one adds most of its weights to the background region. This phe-

nomenon happens in all the models from different view-points and different folds, which implies our approach is able to capture multi-stage visual cues and this indeed improves segmentation accuracy. We note that a similar conclusion is also drawn in image classification (Zhu, Xie, and Yuille 2017), *i.e.*, except for foreground, background and boundary also contribute to visual recognition.

The Benefits of Joint Training

Next, we investigate the benefit of our joint optimization framework. For this, we argue that both the coarse-scaled and fine-scaled segmentation networks become stronger. We denote the coarse-scaled and fine-scaled networks trained individually as \mathbb{I}^C and \mathbb{I}^F , and similarly, those trained in a joint manner as \mathbb{J}^C and \mathbb{J}^F , respectively.

We first observe the coarse-scaled segmentation results. The original individually-trained coarse-scaled networks reported an average accuracy of 75.74%, and the coarse-scaled

networks decomposed from our jointly-optimized model achieves 78.23%, which is considerably higher. To evaluate the fine stage, we mix the individually-trained models and the jointly-optimized models in the testing phase. Using \mathbb{I}^C and \mathbb{J}^F together achieves an 83.80% accuracy. Note that the baseline and our approach can be represented as \mathbb{I}^C - \mathbb{I}^F and \mathbb{J}^C - \mathbb{J}^F , and the corresponding numbers are 82.37% and 84.50%, respectively. From these numbers, we conclude that both the coarse-scaled and fine-scaled networks become more accurate via joint optimization, *i.e.*, the coarse stage provides a better starting point, and the fine stage also works better during iteration.

Convergence

We evaluate convergence of the coarse-to-fine iteration. As elaborated in (Zhou et al. 2016), this is a very important criterion to judge the reliability of our approach. We choose the best model reporting an 84.50% average accuracy, and record the inter-iteration DSC (the DSC between volumes of two consecutive iterations) after each round of iteration.

After 1, 2, 3, 5 and 10 rounds, these numbers are 0.9037, 0.9677, 0.9814, 0.9908 and 0.9964 for our approach, and 0.8286, 0.9477, 0.9661, 0.9743 and 0.9774 for (Zhou et al. 2016), respectively. Each number reported by our approach is considerably higher than the corresponding one by (Zhou et al. 2016). The better convergence property provides us with the opportunity to set a more strict terminating condition, *e.g.*, using $t = 0.99$ rather than $t = 0.95$, so as the stability is better guaranteed. We note that (Zhou et al. 2016) also tried to increase the threshold from 0.95 to 0.99, but only 3 out of 82 cases converged after 10 rounds, and the average accuracy goes down from 82.37% to 82.28%. In contrary, when we increase the threshold from 0.95 to 0.99, convergence happens on 80 out of 82 cases, with an average of 5.22 rounds, and the average accuracy is improved from 83.93% to 84.50%. In addition, the average number of rounds needed to achieve $t = 0.95$ is reduced from 2.89 in (Zhou et al. 2016) to 2.02 in our approach. Using $t = 0.99$ increases the number of iterations and, consequently, computational overheads in the testing phase. In average, each case requires around 1.3 minutes (50% longer than using $t = 0.95$), which is acceptable.

The Over-Fitting Issue

Finally, we investigate the over-fitting issue by making use of *oracle* information in the testing process. We follow (Zhou et al. 2016) to use the ground-truth bounding box *on each slice*, which is expensive to annotate and thus not applicable in real-world clinical applications. In our approach, the oracle bounding boxes can be used for both image cropping and spatial weighting, or only for image cropping. The first scenario is named the *strong oracle*, in which no iteration is required, while the second scenario is named the *weak oracle*, in which we still need to perform iteration till convergence.

Based on our best model which reports an 84.50% average accuracy, using the strong oracle achieves an average accuracy of 91.42%, and the weak oracle also reports 86.37%, both of which are much higher than the number without

using oracle information. If we do not fine-tune the networks using noisy data (see Table 1), the above numbers are 83.68% (no oracle used), 91.29% and 86.26%, respectively. This is to say, the fine-tuning strategy not only improves segmentation accuracy by nearly 1%, but also alleviates the over-fitting phenomenon (the disadvantages from those oracle models become smaller).

Conclusions

In this paper, we present the **Saliency Transformation Network** for coarse-to-fine organ segmentation from abdominal CT scans. Our approach is motivated by the previous method (Zhou et al. 2016), which deals with the two segmentation stages individually, so that it is difficult to make use of multi-stage visual cues to improve segmentation accuracy. We insert a saliency transformation module, so that the coarse-scaled segmentation result can be propagated to the fine stage as spatial weights. This allows us to jointly optimize these two networks and both of them become more accurate. With the same testing process, our approach outperforms the baseline by an average of more than 2%. This improvement is possibly brought by the complementary information delivered by saliency transformation. The diagnostic experiments also show several promising properties of our approach such as better convergence.

Acknowledgements

This work was supported by the Lustgarten Foundation for Pancreatic Cancer Research. We thank Song Bai, Zhuotun Zhu and Siyuan Qiao for instructive discussions.

References

- Ali, A.; Farag, A.; and El-Baz, A. 2007. Graph Cuts Framework for Kidney Segmentation with Prior Shape Constraints. *International Conference on Medical Image Computing and Computer-Assisted Intervention*.
- Cai, J.; Lu, L.; Xie, Y.; Xing, F.; and Yang, L. 2017. Improving Deep Pancreas Segmentation in CT and MRI Images via Recurrent Neural Contextual Learning and Direct Loss Function. *arXiv preprint arXiv:1707.04912*.
- Chen, L.; Papandreou, G.; Kokkinos, I.; Murphy, K.; and Yuille, A. 2015. Semantic Image Segmentation with Deep Convolutional Nets and Fully Connected CRFs. *International Conference on Learning Representations*.
- Chen, H.; Dou, Q.; Wang, X.; Qin, J.; and Heng, P. 2016a. Mitosis Detection in Breast Cancer Histology Images via Deep Cascaded Networks. *AAAI Conference on Artificial Intelligence*.
- Chen, L.; Yang, Y.; Wang, J.; Xu, W.; and Yuille, A. 2016b. Attention to Scale: Scale-aware Semantic Image Segmentation. *Computer Vision and Pattern Recognition*.
- Dou, Q.; Chen, H.; Jin, Y.; Yu, L.; Qin, J.; and Heng, P. 2016. 3D Deeply Supervised Network for Automatic Liver Segmentation from CT Volumes. *International Conference on Medical Image Computing and Computer-Assisted Intervention*.

- Girshick, R.; Donahue, J.; Darrell, T.; and Malik, J. 2014. Rich Feature Hierarchies for Accurate Object Detection and Semantic Segmentation. *Computer Vision and Pattern Recognition*.
- Harrison, A.; Xu, Z.; George, K.; Lu, L.; Summers, R.; and Mollura, D. 2017. Progressive and Multi-Path Holistically Nested Neural Networks for Pathological Lung Segmentation from CT Images. *International Conference on Medical Image Computing and Computer-Assisted Intervention*.
- Havaei, M.; Davy, A.; Warde-Farley, D.; Biard, A.; Courville, A.; Bengio, Y.; Pal, C.; Jodoin, P.; and Larochelle, H. 2017. Brain Tumor Segmentation with Deep Neural Networks. *Medical Image Analysis*.
- He, K.; Zhang, X.; Ren, S.; and Sun, J. 2016. Deep Residual Learning for Image Recognition. *Computer Vision and Pattern Recognition*.
- Heimann, T.; Van Ginneken, B.; Styner, M.; Arzhaeva, Y.; Aurich, V.; Bauer, C.; Beck, A.; Becker, C.; Beichel, R.; Bekes, G.; et al. 2009. Comparison and Evaluation of Methods for Liver Segmentation from CT Datasets. *IEEE Transactions on Medical Imaging* 28(8):1251–1265.
- Hu, S.; Hoffman, E.; and Reinhardt, J. 2001. Automatic Lung Segmentation for Accurate Quantitation of Volumetric X-ray CT Images. *IEEE Transactions on Medical Imaging* 20(6):490–498.
- Kamnitsas, K.; Ledig, C.; Newcombe, V.; Simpson, J.; Kane, A.; Menon, D.; Rueckert, D.; and Glocker, B. 2016. Efficient Multi-Scale 3D CNN with Fully Connected CRF for Accurate Brain Lesion Segmentation. *arXiv preprint arXiv:1603.05959*.
- Krizhevsky, A.; Sutskever, I.; and Hinton, G. 2012. ImageNet Classification with Deep Convolutional Neural Networks. *Advances in Neural Information Processing Systems*.
- Lai, M. 2015. Deep Learning for Medical Image Segmentation. *arXiv preprint arXiv:1505.02000*.
- Lin, D.; Lei, C.; and Hung, S. 2006. Computer-Aided Kidney Segmentation on Abdominal CT Images. *IEEE Transactions on Information Technology in Biomedicine* 10(1):59–65.
- Ling, H.; Zhou, S.; Zheng, Y.; Georgescu, B.; Suehling, M.; and Comaniciu, D. 2008. Hierarchical, Learning-based Automatic Liver Segmentation. *Computer Vision and Pattern Recognition*.
- Linguraru, M.; Sandberg, J.; Li, Z.; Shah, F.; and Summers, R. 2010. Automated Segmentation and Quantification of Liver and Spleen from CT Images Using Normalized Probabilistic Atlases and Enhancement Estimation. *Medical Physics* 37(2):771–783.
- Long, J.; Shelhamer, E.; and Darrell, T. 2015. Fully Convolutional Networks for Semantic Segmentation. *Computer Vision and Pattern Recognition*.
- Merkow, J.; Kriegman, D.; Marsden, A.; and Tu, Z. 2016. Dense Volume-to-Volume Vascular Boundary Detection. *International Conference on Medical Image Computing and Computer-Assisted Intervention*.
- Milletari, F.; Navab, N.; and Ahmadi, S. 2016. V-Net: Fully Convolutional Neural Networks for Volumetric Medical Image Segmentation. *arXiv preprint arXiv:1606.04797*.
- Ren, S.; He, K.; Girshick, R.; and Sun, J. 2015. Faster R-CNN: Towards Real-time Object Detection with Region Proposal Networks. *Advances in Neural Information Processing Systems*.
- Ronneberger, O.; Fischer, P.; and Brox, T. 2015. U-Net: Convolutional Networks for Biomedical Image Segmentation. *International Conference on Medical Image Computing and Computer-Assisted Intervention*.
- Roth, H.; Lu, L.; Farag, A.; Shin, H.; Liu, J.; Turkbey, E.; and Summers, R. 2015. DeepOrgan: Multi-level Deep Convolutional Networks for Automated Pancreas Segmentation. *International Conference on Medical Image Computing and Computer-Assisted Intervention*.
- Roth, H.; Lu, L.; Farag, A.; Sohn, A.; and Summers, R. 2016. Spatial Aggregation of Holistically-Nested Networks for Automated Pancreas Segmentation. *International Conference on Medical Image Computing and Computer-Assisted Intervention*.
- Roth, H.; Lu, L.; Lay, N.; Harrison, A.; Farag, A.; Sohn, A.; and Summers, R. 2017. Spatial Aggregation of Holistically-Nested Convolutional Neural Networks for Automated Pancreas Localization and Segmentation. *arXiv preprint arXiv:1702.00045*.
- Simonyan, K., and Zisserman, A. 2015. Very Deep Convolutional Networks for Large-Scale Image Recognition. *International Conference on Learning Representations*.
- Wang, Z.; Bhatia, K.; Glocker, B.; Marvao, A.; Dawes, T.; Misawa, K.; Mori, K.; and Rueckert, D. 2014. Geodesic Patch-based Segmentation. *International Conference on Medical Image Computing and Computer-Assisted Intervention*.
- Wang, D.; Khosla, A.; Gargeya, R.; Irshad, H.; and Beck, A. 2016. Deep Learning for Identifying Metastatic Breast Cancer. *arXiv preprint arXiv:1606.05718*.
- Xia, F.; Wang, P.; Chen, L.; and Yuille, A. 2016. Zoom Better to See Clearer: Human and Object Parsing with Hierarchical Auto-Zoom Net. *European Conference on Computer Vision*.
- Zhang, Y.; Ying, M.; Yang, L.; Ahuja, A.; and Chen, D. 2016. Coarse-to-Fine Stacked Fully Convolutional Nets for Lymph Node Segmentation in Ultrasound Images. *IEEE International Conference on Bioinformatics and Biomedicine*.
- Zhou, Y.; Xie, L.; Shen, W.; Wang, Y.; Fishman, E.; and Yuille, A. 2016. Pancreas Segmentation in Abdominal CT Scan: A Coarse-to-Fine Approach. *arXiv preprint arXiv:1612.08230*.
- Zhou, Y.; Xie, L.; Fishman, E.; and Yuille, A. 2017. Deep Supervision for Pancreatic Cyst Segmentation in Abdominal CT Scans. *arXiv preprint arXiv:1706.07346*.
- Zhu, Z.; Xie, L.; and Yuille, A. 2017. Object Recognition with and without Objects. *International Joint Conference on Artificial Intelligence*.